Improper Ferroelectricity in Stuffed Aluminate Sodalites for Pyroelectric Energy Harvesting

Yusaku Maeda,[1] Toru Wakamatsu,[1] Ayako Konishi,[2,3] Hiroki Moriwake,[2,3] Chikako Moriyoshi,[4] Yoshihiro Kuroiwa,[4] Kenji Tanabe,[1] Ichiro Terasaki,[1] and Hiroki Taniguchi[1,*]

[1]*Department of Physics, Nagoya University, Nagoya 464-8602, Japan*
[2]*Nanostructures Research Laboratory, Japan Fine Ceramics Center, Nagoya 456-8587, Japan*
[3]*Center for Materials Research by Information Integration (CMI^2) National Institute for Materials Science (NIMS), Tsukuba 305-0047, Japan*
[4]*Department of Physical Science, Hiroshima University, Higashihiroshima 739-8526, Japan*

(Received 8 November 2016; revised manuscript received 26 January 2017; published 24 March 2017)

In the present study, we demonstrate ferroelectricity in stuffed aluminate sodalites $(Ca_{1-x}Sr_x)_8[AlO_2]_{12}(WO_4)_2$ $(x \leq 0.2)$ ($C_{1-x}S_xAW$). Pyroelectric measurements clarify switchable spontaneous polarization in polycrystalline $C_{1-x}S_xAW$, whose polarization values are on the order of 10^{-2} $\mu C/cm^2$ at room temperature. A weak anomaly in the dielectric permittivity at temperatures near the ferroelectric transition temperature suggests improper ferroelectricity of $C_{1-x}S_xAW$ for all investigated values of x. A comprehensive study involving synchrotron x-ray powder diffraction measurements, molecular dynamics simulations, and first-principles calculations clarifies that the ferroelectric phase transition of $C_{1-x}S_xAW$ is driven by the freezing of the fluctuations of WO_4 tetrahedra in the voids of an $[AlO_2]_{12}{}^{12-}$ framework. The voltage response and electromechanical coupling factor of $C_{1-x}S_xAW$ estimated from the present results indicate that this material exhibits excellent performance as a pyroelectric energy harvester, suggesting that aluminate sodalites exhibit great promise as a class of materials for highly efficient energy-harvesting devices.

DOI: 10.1103/PhysRevApplied.7.034012

I. INTRODUCTION

Inducing a polar ground state is an intriguing issue in solid-state physics, materials science, and inorganic chemistry because the polar symmetry provides a unique background for various functionalities [1]. One representative example is ferroelectricity, which features switchable spontaneous polarization, pyroelectricity, piezoelectricity, and nonlinear optical responses and is applied in state-of-the-art technologies. Ferroelectric oxides have conventionally been developed with oxygen-octahedra-based compounds typified by perovskite-type ferroelectrics such as $Pb(Zr, Ti)O_3$, $BaTiO_3$, and $LiNbO_3$. Several effects play important roles in inducing ferroelectricity in octahedra-based oxides: A second-order Jahn-Teller effect gives rise to polar displacements of cations in the oxygen octahedra [2–8]. A steric hindrance effect of specific elements with a lone electron pair, by contrast, displaces the atom from the centric position among surrounding ligand oxygens to render the crystal noncentrosymmetric [9,10]. Furthermore, recent studies suggest that multiple instabilities of octahedral rotations cooperatively induce ferroelectricity [11–15].

In contrast to the numerous investigations of oxygen-octahedra-based ferroelectric compounds, the literature contains few reports of ferroelectricity in oxygen-tetrahedra-based compounds other than hydrogen-bonded compounds [16], which are often unsuitable for practical applications because they deliquesce. Because oxygen-tetrahedra-based compounds are abundant in Earth's crust, as typified by quartz and zeolites, the development of ferroelectric oxygen-tetrahedra-based compounds should lead to innovative ecofriendly devices. Recently, Taniguchi *et al.* [17] reported excellent ferroelectricity in Bi_2SiO_5, an oxygen-tetrahedra-based silicate. The ferroelectricity in Bi_2SiO_5 is driven by twisting deformations of one-dimensional chains of SiO_4 tetrahedra that partially compose the crystal structure [17–19]. Furthermore, the switchable spontaneous polarization of approximately 23 $\mu C/cm^2$, which is comparable to that of perovskite-type ferroelectric oxides, is induced by internal deformation of SiO_4 tetrahedra [17,18,20]. The discovery of ferroelectricity in Bi_2SiO_5 has opened a path for the development of ferroelectric oxides through exploitation of oxygen-tetrahedra networks.

An aluminate sodalite-type oxide is an oxygen-tetrahedra-based oxide of the sodalite family [21]. It possesses an $[AlO_2]_{12}{}^{12-}$ framework structure composed of AlO_4 tetrahedra. The $[AlO_2]_{12}{}^{12-}$ framework has two inequivalent voids occupied by alkaline-earth divalent cations and $(MO_4)^{2-}$ (M = S, Cr, Mo, W) tetrahedral anions, resulting in a chemical composition of $Ae_8[AlO_2]_{12}(MO_4)_2$

*Corresponding author.
hiroki_taniguchi@cc.nagoya-u.ac.jp

(*Ae* denotes an alkaline-earth element). The aluminate sodalite-type oxides undergo various structural phase transitions because of the underlying lattice instability in their network of oxygen tetrahedra [22–24]. $Sr_8[AlO_2]_{12}(CrO_4)_2$, in particular, has been reported to undergo a ferroelectric phase transition at T_c of approximately 300 K [25]. A small spontaneous polarization and a weak dielectric anomaly observed at approximately T_c indicate an improper ferroelectric phase transition of $Sr_8[AlO_2]_{12}(CrO_4)_2$, whose primary order parameter is not polarization but another physical quantity. Such improper ferroelectricity has recently been attracting increasing attention because of its potential for multifunctionalities based on intimate coupling between the polarization and another physical quantity, as observed in the case of multiferroic materials [26,27]. The aluminate sodalite-type oxides represent a frontier in the development of oxygen-tetrahedra-based ferroelectric oxides.

Here, we report improper ferroelectricity in $(Ca_{1-x}Sr_x)_8[AlO_2]_{12}(WO_4)_2$ $(0 \le x \le 0.2)$, which is abbreviated hereafter as $C_{1-x}S_xAW$. Pyroelectric measurements demonstrate switchable spontaneous polarization on the order of 10^{-2} $\mu C/cm^2$, which is comparable to that of conventional improper ferroelectric oxides [28]. Molecular dynamics simulations indicate that strong fluctuations of WO_4 tetrahedra in the voids of the $[AlO_2]_{12}{}^{12-}$ framework freeze to drive the improper ferroelectric phase transition. First-principles calculations clarify that the fluctuation of WO_4 tetrahedra stems from multiple instabilities at finite wave numbers in acoustic phonon branches. Although its magnitude of spontaneous polarization is small, $C_{1-x}S_xAW$ is found to possess strong potential for use in pyroelectric energy harvesters because of its small dielectric permittivity even at temperatures near the ferroelectric phase-transition temperature. The present study sheds light on the development of oxygen-tetrahedra-based ferroelectric materials with potential applications in high-performance energy-harvesting devices.

II. EXPERIMENT

To synthesize polycrystalline samples of $C_{1-x}S_xAW$, stoichiometric mixtures of $CaCO_3$, $SrCO_3$, WO_3, and Al_2O_3 are heated at 1673 K for 12 h, followed by furnace cooling. Powder x-ray diffraction (PXRD) measurements confirm that all samples are in a single-phase state with no impurity phases. Differential scanning calorimetry (DSC) is carried out on a DSC 8230 (Thermo Plus Co.) to investigate the phase-transition temperature. Dielectric permittivity is measured from room temperature to 700 K using a Keysight 4284A precision *LCR* meter. The temperature dependence of the spontaneous polarization is obtained through measurement of the pyrocurrent during zero-field heating after poling by field cooling using a bias field of 10 kV/cm. PXRD analyses are performed on the powder diffraction beam line BL02B2 at SPring-8 with the approval of the Japan Synchrotron Radiation Research Institute of SPring-8. The wavelengths of incident x rays used in the present study are 18 keV (0.67 Å) and 30 keV (0.41 Å).

First-principles calculations are performed within the framework of density-functional theory (DFT) using the projector-augmented-wave method [29] as implemented in the VASP code [30]. A plane-wave cutoff energy of 500 eV and a $4 \times 4 \times 4$ k-point mesh are used. We also carry out systematic first-principles molecular dynamics (FPMD) simulations within the *NVT* ensemble using the Nosé thermostat [31]. The time step is 1 fs. Simulation cells contain 54 atoms (i.e., 1 formula unit). The lattice volume optimized by DFT calculations for the high-temperature $I4\bar{3}m$ phase is used for all of the FPMD calculations.

III. RESULTS AND DISCUSSION

The $C_{1-x}S_xAW$ is composed of an $[AlO_2]_{12}{}^{12-}$ framework with two nonequivalent voids filled by $Ca^{2+}(Sr^{2+})$ and $WO_4{}^{2-}$ [Fig. 1(a)]. As shown in Fig. 1(b), one of the end members $C_{1-x}S_xAW$ $(x = 0)$ undergoes a successive high-temperature structural phase transition from a centrosymmetric $I4\bar{3}m$ phase (α phase) to a noncentrosymmetric $Aba2$ phase (γ phase) through an intermediate incommensurate phase (β phase), which has been previously reported to exist in a narrow temperature range between the $I4\bar{3}m$ and $Aba2$ phases [32]. The other end member $C_{1-x}S_xAW$ $(x = 1)$, by contrast, has a high-temperature $Im\bar{3}m$ phase, and the structure transforms to $I4_1/acd$ at approximately 600 K with decreasing temperature [33]. Figures. 1(b) and 1(c) show the phase diagram of $C_{1-x}S_xAW$ for $0 \le x \le 0.20$, as constructed on the basis of the results of DSC and PXRD analyses. Solid circles, triangles, and squares are the transition temperatures determined by DSC measurements upon heating. The corresponding open symbols are determined upon cooling. The plusses, crosses, and diamonds indicate the α, γ, and γ' phases, respectively, assigned on the basis of the powder x-ray diffraction measurements. The broken curves in the panels denote eye guides for the solidus curves. The present results are in good agreement with those previously report by Többens and Deppmeier [32].

Figure 2 shows the temperature dependence of dielectric permittivity for $C_{1-x}S_xAW$ $(x = 0, 0.03, 0.10, 0.16)$. The squares, circles, triangles, and crosses indicate results for $x = 0$, 0.03, 0.10, and 0.16, respectively. The solid, broken, and chain lines in the figure, respectively, denote the horizontal axes for $x = 0.03$, 0.10, and 0.16, whose levels are systematically raised for visibility. The arrows in the figure denote several dielectric anomalies indicating the phase transitions in $C_{1-x}S_xAW$. At $x = 0$, a successive phase transition is detected at temperatures above 600 K. The phase-transition temperature decreases upon Sr substitution at $x = 0.03$. With further substitution, $C_{1-x}S_xAW$ undergoes a single-phase transition, consistent with the

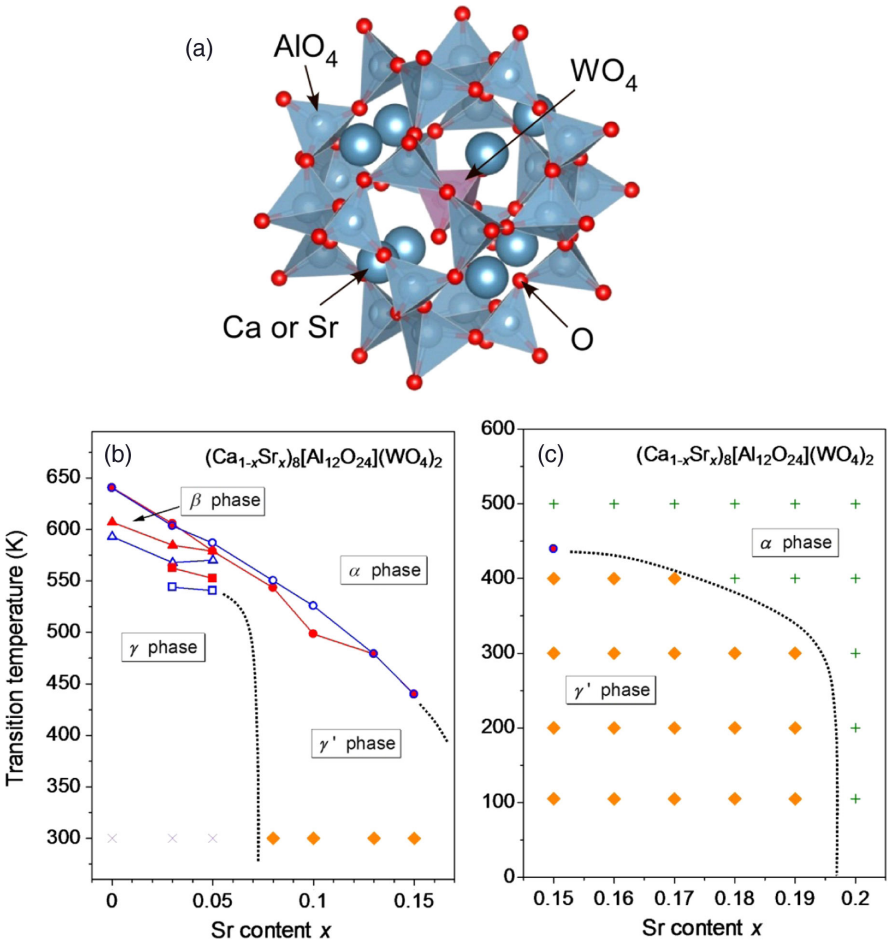

FIG. 1. (a) The crystal structure and phase diagram of $C_{1-x}S_xAW$ over the ranges (b) $0 \le x \le 0.15$ and (c) $0.15 \le x \le 0.20$, as determined by DSC and powder x-ray diffraction measurements in the present study.

phase diagram constructed on the basis of the DSC measurements. Notably, the dielectric permittivity of $C_{1-x}S_xAW$ shows a subtle temperature variation even around the phase-transition temperature and remains below

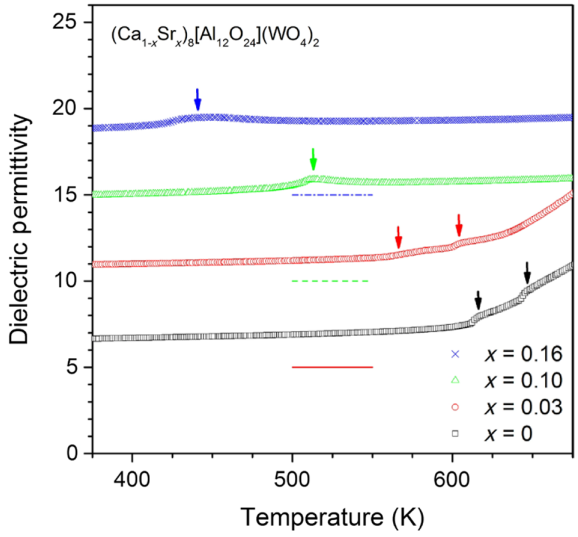

FIG. 2. The temperature dependence of dielectric permittivity for $C_{1-x}S_xAW$. Data points for $x = 0$, 0.03, 0.10, and 0.16 are plotted as squares, circles, triangles, and crosses, respectively. See text for details.

$\varepsilon' \approx 10$ over the entire investigated temperature range in the present study. This behavior contrasts sharply with that for a *proper* ferroelectric phase transition, which generally shows a divergent increase of the dielectric permittivity at temperatures near the phase-transition temperature.

Figure 3 shows the temperature dependence of the spontaneous polarization for $C_{1-x}S_xAW$ ($x = 0.03$, 0.10, 0.16). The circles, triangles, and crosses in the figure denote the results for $x = 0.03$, 0.10, and 0.16, respectively. The data for $x = 0$ are not shown because the pyroelectric measurements for $C_{1-x}S_xAW$ at $x = 0$ are unsuccessful as a consequence of its high transition temperature. We observe positive and negative spontaneous polarizations when opposite bias fields are applied during the field-cooling processes in the pyroelectric measurements, indicating switchable spontaneous polarization of $C_{1-x}S_xAW$. In the composition with $x = 0.03$, as denoted by the circles in Fig. 3, a two-step increase in the spontaneous polarization is observed at approximately 600 and 580 K, corresponding to the successive phase transition. An increase of the Sr content x suppresses the formation of the intermediate phase between these two transition temperatures, as also clarified by the DSC and dielectric measurements. The value of the spontaneous polarization

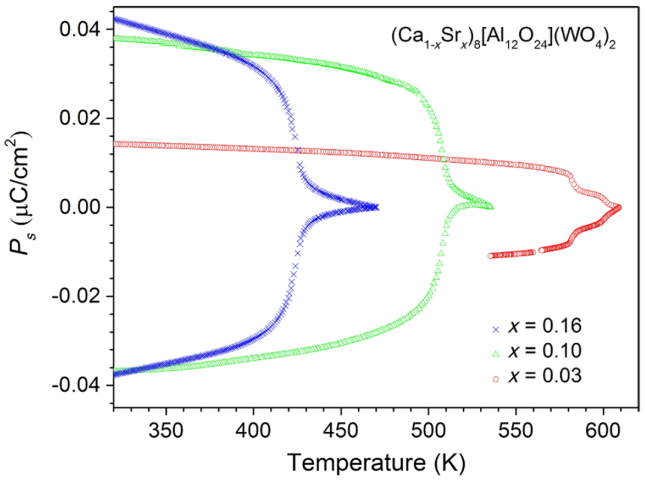

FIG. 3. The temperature dependence of spontaneous polarization for $C_{1-x}S_xAW$. Data points for $x = 0.03$, 0.10, and 0.16 are plotted as circles, triangles, and crosses, respectively. See text for details.

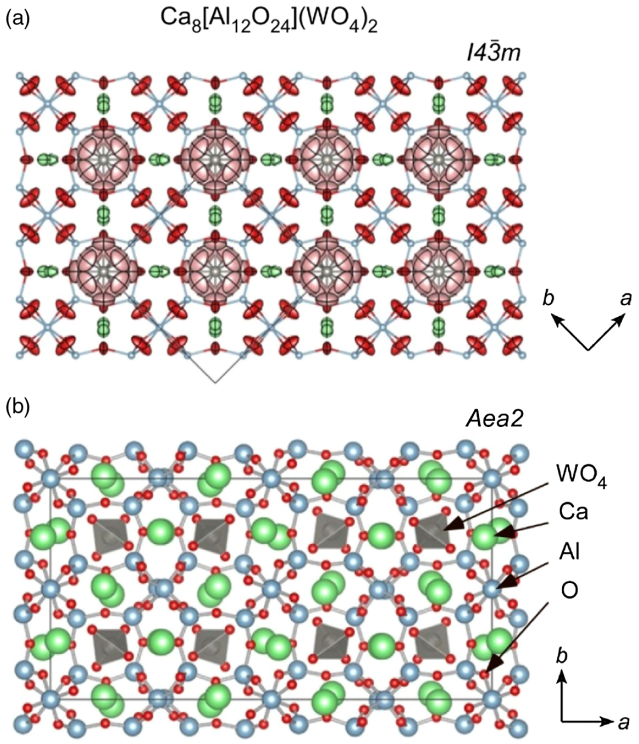

FIG. 4. The crystal structures of $C_{1-x}S_xAW$ in (a) the highest- and (b) lowest-temperature phases, as determined by structural analyses using powder x-ray diffraction measurements. Solid squares in the panels denote the unit cells for both phases.

at room temperature, however, increases with x, reaching 0.04 $\mu C/cm^2$ at $x = 0.16$. This value is much smaller than that of conventional ferroelectric oxides [16]. Such a small spontaneous polarization is often observed in so-called *improper* ferroelectrics, as represented by $Gd_2(MoO_4)_3$ and the multiferroic $TbMnO_3$ [26,28]. The small spontaneous polarization and the weak dielectric anomaly at temperatures near the phase-transition temperature indicate improper ferroelectricity in $C_{1-x}S_xAW$.

Here, we briefly discuss structural aspects of the phase transition of $C_{1-x}S_xAW$ by analyzing the structural variations of $C_{1-x}S_xAW$ ($x = 0$) through the phase transitions. Figure 4 presents the crystal structures of the highest-symmetry phase $I\bar{4}3m$ [Fig. 4(a)] and the lowest-symmetry phase $Aea2$ [Fig. 4(b)] observed at 700 and 300 K, respectively. The squares in the panels denote the unit cells in the phases. The anisotropic thermal vibration is expressed by thermal ellipsoids only for the highest-symmetry phase. In the highest-symmetry phase, as shown in Fig. 4(a), each WO_4 tetrahedron is in a disordered state among six equivalent orientations in the void of the $[AlO_2]_{12}{}^{12-}$ framework [22]. The expanded thermal ellipsoids, furthermore, indicate that the potential barriers separating each orientation are smooth, rendering the motion of the WO_4 tetrahedra almost rotatory. In synchronization with the disordering of WO_4 tetrahedra, the $[AlO_2]_{12}{}^{12-}$ framework liberates the distortions associated with each orientation of WO_4 tetrahedra. Ca^{2+} cations, by contrast, have small thermal ellipsoids, suggesting that their thermal fluctuations are relatively weak. In the lowest-symmetry phase, as shown in Fig. 4(b), the WO_4 tetrahedra settle at each orientation. The ordering of the WO_4 orientation should play an essential role in the phase transition of $C_{1-x}S_xAW$.

To clarify the dynamical aspect of the phase transition in $C_{1-x}S_xAW$, we perform molecular dynamics simulations. Figure 5 shows traces of WO_4 motions calculated at (left) 1000 K, (center) 700 K, and (right) 300 K. The yellow dots in the figure indicate the variations of the positions for apical oxygens in the WO_4 tetrahedra with time. As evident in the figure, the trace of the apical oxygens is found to spread around the tungsten cation in the void of the $[AlO_2]_{12}{}^{12-}$ framework at 1000 K. This spherical distribution of apical oxygens indicates that WO_4 tetrahedra rotate almost freely because of the smooth potential barriers at high temperatures. As the temperature decreases to 700 K, as shown in the figure, the spatial distribution of apical oxygens condenses over four positions around the tungsten cation, suggesting ordering of the WO_4 orientation. Although the ordering temperature is slightly different from that observed in the experiments, likely because of the limited accuracy of the present calculations, the results of the molecular dynamics simulations clearly demonstrate that the phase transition of $C_{1-x}S_xAW$ is driven by the freezing of the nearly free rotation of WO_4 tetrahedra in the voids of the $[AlO_2]_{12}{}^{12-}$ framework. Furthermore, with a further decrease of the temperature to 300 K, the distribution of apical oxygens becomes more localized, indicating that the fluctuation of WO_4 weakens in an ordered orientation. Notably, the phase transition to the intermediate phase is not addressed in the present study.

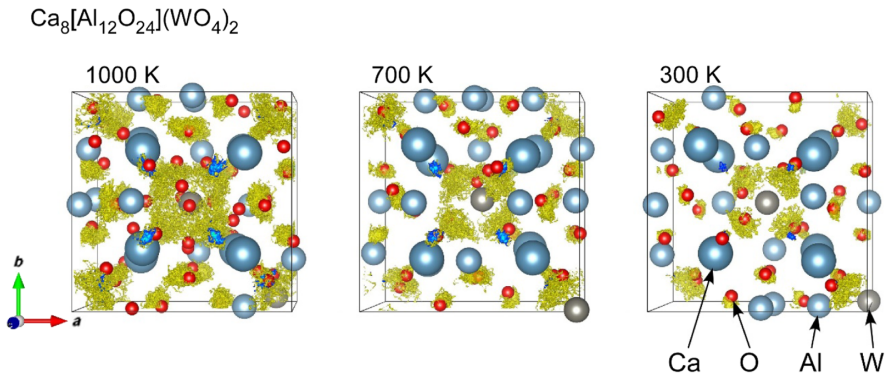

FIG. 5. The fluctuation of WO_4 tetrahedra in the void of the $[AlO_2]_{12}^{12-}$ framework at 1000 (left), 700 (center), and 300 K (right), as calculated using molecular dynamics simulations for $C_{1-x}S_xAW$ with $x = 0$. The yellow dots in the figure indicate variations of positions for the apical oxygens in the WO_4 tetrahedra with time.

To better understand the phase transition of $C_{1-x}S_xAW$, we investigate the lattice dynamics by first-principles calculations. Figure 6 shows the phonon dispersion in $C_{1-x}S_xAW$ at $x = 0$ calculated in the $I4\bar{3}m$ structure at zero temperature, where the area below zero frequency in the vertical axis indicates imaginary frequency. The results show that several acoustic phonon branches have imaginary frequencies around the Z, X, and N points in the Brillouin zone. Such unstable phonon modes with imaginary frequency are called "soft modes," and their freezing is known to induce structural phase transitions [16]. The displacement patterns of all of these unstable lattice vibrations are observed to have common characteristics involving WO_4 tetrahedra vibrations of substantial amplitude. The nearly rotatory fluctuation of WO_4 tetrahedra clarified by the molecular dynamics simulations is composed of these modes, which acquire stable vibrations through thermal fluctuations. As the temperature decreases, the frequencies of these modes decrease because of suppression of thermal fluctuations; these modes (or one of them) eventually freeze, triggering the structural phase transition. From this perspective, we can interpret the phase transition of $C_{1-x}S_xAW$ as being soft-mode driven. Notably, we ignore the imaginary frequency branch between the P and Γ points because the present calculations are not sufficiently accurate to discuss a general point in the Brillouin zone.

We finally discuss the potential application of $C_{1-x}S_xAW$ for pyroelectric energy harvesting. Among several pyroelectric energy-harvesting cycles reported so far [34–37], we focus on the performance of $C_{1-x}S_xAW$ for the synchronized electric-charge-extraction (SECE) cycle,

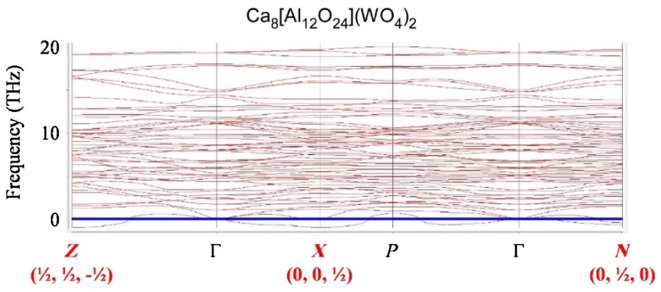

FIG. 6. Phonon-dispersion curves for $C_{1-x}S_xAW$ ($x = 0$), as calculated from first principles.

since the SECE cycle can generate electronic energy basically from the temperature variation alone without applying external voltage and is one of the most natural cycles from the viewpoint of the thermodynamics [36]. In this cycle, two parameters are used to characterize the performance of pyroelectric energy-harvesting materials: the electromechanical coupling factor and the voltage response. These parameters are defined by $(p^2\theta_h)/(\epsilon' C)$ and $-p/\epsilon'$, respectively, where p is the pyroelectric coefficient at temperature θ_h, ϵ' is the dielectric permittivity, and C is the heat capacity. Figures 7(a) and 7(b) show the temperature dependence of the electromechanical coupling factor and the voltage response of $C_{1-x}S_xAW$ with $x = 0.16$ ($C_{0.84}S_{0.16}AW$). Both factors increase as the temperature reaches the phase-transition temperature. Because the dielectric permittivity of $C_{0.84}S_{0.16}AW$ exhibits little temperature dependence, the observed variations of the electromechanical coupling factor and the voltage response mainly originate from the change in the pyroelectric coefficient with the changing temperature.

To demonstrate the potential for $C_{0.84}S_{0.16}AW$ as a pyroelectric energy harvester, we map its electromechanical coupling factor and voltage response, as shown in Fig. 7(c), along with those for other materials, whose data are extracted from the literature [37]. The results for $C_{0.84}S_{0.16}AW$ are plotted as closed circles in the panel; the closed squares, open squares, closed triangles, and open triangles denote the results for single crystals, the bulk ceramics, the thin films, and several composites of Pb-based ferroelectrics (Pb-based FE), respectively. We note here that the data points for $C_{0.84}S_{0.16}AW$ are obtained using the same sample at different temperatures. The most prominent feature of $C_{0.84}S_{0.16}AW$ is its large voltage response that reaches the larger value than the voltage responses of the other systems represented in the figure by several orders of magnitude. The voltage response represents a conversion efficiency from the polarization variation to the electric field. In the SECE pyroelectric energy-harvesting cycles, the variation of spontaneous polarization is converted to the electric field via $\Delta D(= \Delta P_S) = \epsilon' \Delta E$ to do the work to the outside, where ΔD and ΔE are variations of electric displacement and electric field, respectively [37]. The small permittivity is, thus,

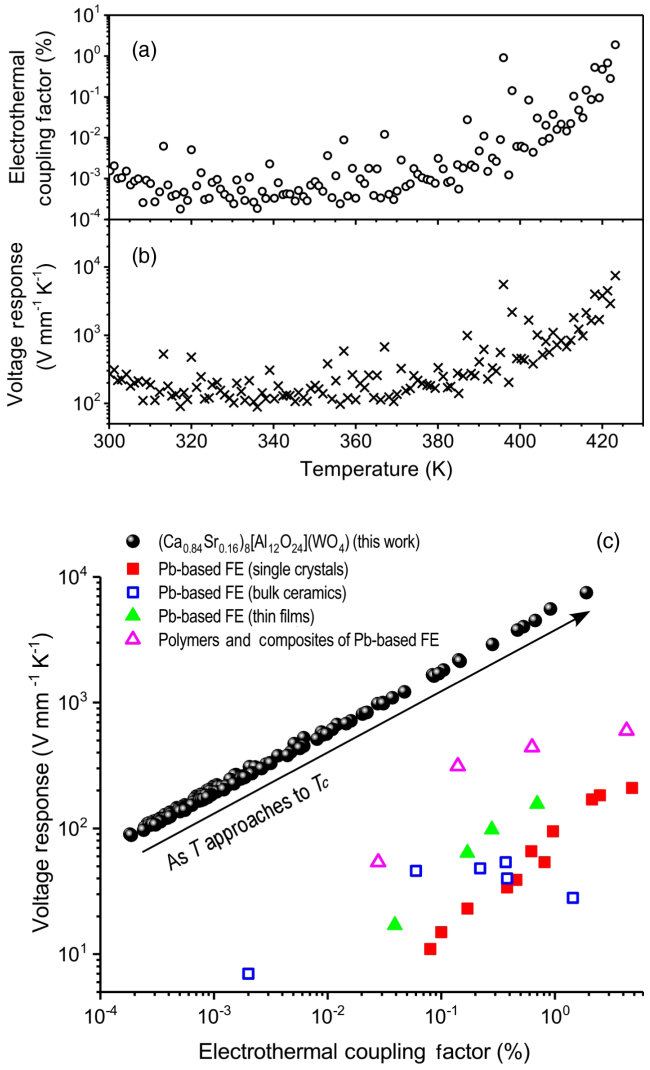

FIG. 7. (a) The electromechanical coupling factor and (b) voltage response of $C_{1-x}S_xAW$ ($x = 0.16$) estimated from the dielectric permittivity and the pyroelectric coefficient measured in the present study. The performance of $C_{1-x}S_xAW$ ($x = 0.16$) as pyroelectric energy harvesters is plotted by closed circles in panel (c) and is compared with the performance of other materials of several forms. The closed squares, open squares, and closed triangles denote the results for single crystals, bulk ceramics, and thin films of several Pb-based FE, including (1-x)$Pb(Mg_{1/3}Nb_{2/3})O_3$-$xPbTiO_3$(PMN-PT), (1-x)Pb$(Zn_{1/3}Nb_{2/3})O_3$-$xPbTiO_3$ (PZN-PT), $PbZr_{1-x}Ti_xO_3$(PZT), and $Pb_{1-y}La_yZr_{1-x}Ti_xO_3$(PLZT), respectively. Open triangles, on the contrary, present the results for ferroelectric polymers and their composites with Pb-based FE, including PVDF, PZT/P(VDF-TrFE), PZT/PVCD-HFP, and PZT/PU (see Ref. [37]). The present results for CSAM-16 ceramics are indicated by closed circles.

advantageous for the induction of electric field to push up the voltage response of the materials. In the case of the proper ferroelectric materials such as Pb-based FE, in general, the dielectric permittivity divergently develops as the temperature approaches T_C. The huge permittivity in temperatures around T_C thereby screens the large ΔP_S of the proper ferroelectric that is generated by the temperature variation, leading to suppress the induced electric field, deteriorating the voltage response. In contrast to the proper ferroelectrics, the permittivity of the improper ferroelectrics exhibits little temperature variation even near the phase-transition temperature, just below which the pyroelectric coefficient p becomes maximum. This behavior dramatically enhances the voltage response in the vicinity of T_C as indicated by the arrow in Fig. 7(c). Such stable dielectric permittivity is specific to improper ferroelectric materials and can never be attained with proper ferroelectric materials. As for the electrothermal coupling factor, the largest value of 4.8% is obtained with the Pb-based ferroelectric single crystal, 0.75PMN-0.25PT, and the PZT/PVCD-HFP composite also achieves the excellent coupling factor of 4.3% as presented in Fig. 7(c). On the other hand, the electromechanical coupling factor in $C_{0.84}S_{0.16}AW$ ceramics is found to reach 2%. Though this value is almost half of the best value in the single crystals and the composites, it is comparable to that for the Pb-based ferroelectric ceramics materials having the same form as that for the $C_{0.84}S_{0.16}AW$ in the present study, suggesting a potential of the improper ferroelectrics for the pyroelectric energy harvesters. This fairly large electrothermal coupling factor in $C_{0.84}S_{0.16}AW$ also stems from its small permittivity even in temperatures near T_C, as indicated by the definition of the electrothermal coupling factor $(p^2\theta_h)/(\epsilon' C)$, where the permittivity is in the denominator.

For the development of the efficient pyroelectric energy harvesters, previous studies focused on the large pyroelectric coefficient of proper ferroelectrics, and several approaches were proposed to enhance their pyroelectric coefficient, for instance, operations in temperatures near T_C [38,39] and miniaturizing materials to nanoscale [40]. However, conventional proper ferroelectrics with large spontaneous polarization are often composed of toxic elements as represented by Pb-based FE. The development of environment-friendly ferroelectric materials has, thus, been an associated issue to be solved for the development of efficient pyroelectric energy harvesting with the proper ferroelectrics [41,42]. The pyroelectric activity with small dielectric permittivity that is realized in the improper ferroelectrics provides an alternative approach to designing pyroelectric energy harvesters of excellent performance. In contrast, the proper ferroelectrics, whose increasing permittivity counterbalances the large spontaneous polarization in the vicinity of T_C, the small and temperature-stable permittivity in the improper ferroelectrics never compensate the enhancement of the pyroelectric coefficient on approaching T_C. The improper ferroelectrics, thus, attains comparable performance for the pyroelectric energy harvesting to the Pb-based FE, though the pyroelectric coefficient itself is small. The improper ferroelectric aluminate sodalities, furthermore, do not contain toxic elements and have intrinsically good environmental

affinity. We believe that enlarging the pyroelectric coefficient of aluminate sodalites is the key to the further development of improper ferroelectric materials for pyroelectric energy harvesting.

IV. CONCLUSION

In summary, we demonstrate the ferroelectricity of $C_{1-x}S_xAW$ by observing switchable spontaneous polarization via pyroelectric measurements. The small spontaneous polarization and weak dielectric anomaly even at temperatures near the phase-transition temperature indicate the improper nature of the ferroelectricity in $C_{1-x}S_xAW$. Our comprehensive study involving structural analyses, molecular dynamics simulations, and first-principles calculations clarifies that the phase transition of $C_{1-x}S_xAW$ is driven by the freezing of fluctuating WO_4 tetrahedra among equivalent orientations in the voids of the $[AlO_2]_{12}^{12-}$ framework. The considerably large voltage response with a large electromechanical coupling factor of $C_{1-x}S_xAW$, which is estimated from the present results, demonstrates the strong potential of stuffed aluminate sodalites as pyroelectric energy harvesters as a result of their unique dielectric properties stemming from their improper ferroelectric phase transition. Because stuffed aluminate sodalites are generally composed of abundant and nontoxic elements, the present study provides a path for the development of functional energy-harvesting devices with environmentally friendly oxides.

ACKNOWLEDGMENTS

This work is partially supported by a Grant-in-Aid for Young Scientists (A) (Grant No. 16H06115), the MEXT Element Strategy Initiative Project, Ministry of Education, Culture, Sports, Science and Technology of Japan through the Grants-in-Aid for Scientific Research on Innovative Areas "Nano Informatics" (Grant No. 25106008) from JSPS, MEXT Elements Strategy Initiative to Form Core Research Centers, and the "Materials Research by Information Integration" Initiative (MI^2I) of the Support Program for Starting Up Innovation Hubs from the Japan Science and Technology Agency. The authors thank Professor E. Nishibori, Professor M. Takata, and Professor M. Sakata for their assistance with the Rietveld analysis. The SR experiments are conducted with the approval of the Japan Synchrotron Radiation Research Institute (Proposals No. 2014B1468, No. 2015A1425, and No. 2015A0074).

[1] P. S. Halasyamani and K. R. Poeppelmeier, Noncentrosymmetric oxides, Chem. Mater. **10**, 2753 (1998).

[2] I. B. Bersuker, Pseudo Jahn-Teller Origin of Perovskite Multiferroics, Magnetic-Ferroelectric Crossover, and Magnetoelectric Effects: The $d^0 - d^{10}$ Problem, Phys. Rev. Lett. **108**, 137202 (2012).

[3] R. G. Pearson, Symmetry rule for predicting molecular structures, J. Am. Chem. Soc. **91**, 4947 (1969).

[4] R. G. Pearson, The second-order Jahn-Teller effect, J. Mol. Struct. **103**, 25 (1983).

[5] T. Hughbanks, Superdegenerate electronic energy levels in extended structures, J. Am. Chem. Soc. **107**, 6851 (1985).

[6] R. A. Wheeler, M. H. Whangbo, T. Hughbanks, R. Hoffmann, J. K. Burdett, and T. A. Albright, Symmetric vs. asymmetric linear M-X-M linkages in molecules, polymers, and extended networks, J. Am. Chem. Soc. **108**, 2222 (1986).

[7] M. Kunz and I. D. Brown, Out-of-center distortions around octahedrally coordinated d^0 transition metals, J. Solid State Chem. **115**, 395 (1995).

[8] J. B. Goodenough, Jahn-Teller phenomena in solids, Annu. Rev. Mater. Sci. **28**, 1 (1998).

[9] R. Seshadri and N. A. Hill, Visualizing the role of Bi 6s "lone pairs" in the off-center distortion in ferromagnetic $BiMnO_3$, Chem. Mater. **13**, 2892 (2001).

[10] P. S. Halasyamani, Asymmetric cation coordination in oxide materials: Influence of lone-pair cations on the intra-octahedral distortion in d^0 transition metals, Chem. Mater. **16**, 3586 (2004).

[11] J. M. Perez-Mato, P. Blaha, K. Schwarz, M. Aroyo, D. Orobengoa, I. Etxebarria, and Alberto García, Multiple instabilities in $Bi_4Ti_3O_{12}$: A ferroelectric beyond the soft-mode paradigm, Phys. Rev. B **77**, 184104 (2008).

[12] N. A. Benedek and C. J. Fennie, Hybrid Improper Ferroelectricity: A Mechanism for Controllable Polarization-Magnetization Coupling, Phys. Rev. Lett. **106**, 107204 (2011).

[13] E. Bousquet, M. Dawber, N. Stucki, C. Lichtensteiger, P. Hermet, S. Gariglio, J.-M. Triscone, and P. Ghosez, Improper ferroelectricity in perovskite oxide artificial superlattices, Nature (London) **452**, 732 (2008).

[14] Y. S. Oh, X. Luo, F.-T. Huang, Y. Wang, and S.-W. Cheong, Experimental demonstration of hybrid improper ferroelectricity and the presence of abundant charged walls in $(Ca, Sr)_3Ti_2O_7$ crystals, Nat. Mater. **14**, 407 (2015).

[15] M. J. Pitcher, P. Mandal, M. S. Dyer, J. Alaria, P. Borisov, H. Niu, J. B. Claridge, and M. J. Rosseinsky, Tilt engineering of spontaneous polarization and magnetization above 300 K in a bulk layered perovskite, Science **347**, 420 (2015).

[16] M. E. Lines and A. M. Glass, *Principles and Applications of Ferroelectrics and Related Materials* (Clarendon Press, Oxford, 1977).

[17] H. Taniguchi, A. Kuwabara, J. Kim, Y. Kim, H. Moriwake, S. W. Kim, T. Hoshiyama, T. Koyama, S. Mori, M. Takata, H. Hosono, Y. Inaguma, and M. Itoh, Ferroelectricity driven by twisting of silicate tetrahedral chains, Angew. Chem., Int. Ed. Engl. **52**, 8088 (2013).

[18] Y. Kim, J. Kim, A. Fujiwara, H. Taniguchi, S. W. Kim, H. Tanaka, K. Sugimoto, K. Kato, M. Itoh, H. Hosono, and M. Takata, Hierarchical dielectric orders in layered ferroelectrics Bi_2SiO_5, Int. Union. Crystall. J. **1**, 160 (2014).

[19] J. Park, B. G. Kim, S. Mori, and T. Oguchi, Tetrahedral tilting and ferroelectricity in Bi_2AO_5 (A = Si, Ge) from first principles calculations, J. Solid State Chem. **235**, 68 (2016).

[20] D. Seol, H. Taniguchi, J.-Y. Hwang, M. Itoh, H. Shin, S. Kim, and Y. Kim, Strong anisotropy of ferroelectricity in lead-free bismuth silicate, Nanoscale **7**, 11561 (2015).

[21] R. X. Fischer and W. H. Baur, Symmetry relationships of sodalite (SOD)-type crystal structures, Z. Kristallogr. **224**, 185 (2009).

[22] W. Depmeier, Aluminate sodalites—A family with strained structures and ferroic phase transitions, Phys. Chem. Miner. **15**, 419 (1988).

[23] W. Depmeier and W. Bührer, Aluminate sodalites: $Sr_8[Al_{12}O_{24}](MoO_4)_2$ (SAM) at 293, 423, 523, 623 and 723 K and $Sr_8[Al_{12}O_{24}](WO_4)_2$ (SAW) at 293 K, Acta Crystallogr. Sect. B **47**, 197 (1991).

[24] W. Depmeier, R. Melzer, and X. Hu, Phase transition in $Sr_8[Al_{12}O_{24}](MoO_4)_2$ aluminate sodalite (SAM), Acta Crystallogr. Sect. B **49**, 483 (1993).

[25] J.-F. Rossignol, J.-P. Rivera, P. Tissot, and H. Schmid, Optical, dielectric and DSC studies of "yellow-type" aluminate sodalite $Sr_8[Al_{12}O_{24}](CrO_4)_2$, Ferroelectrics **79**, 197 (1988).

[26] T. Kimura, T. Goto, H. Shintani, K. Ishizaka, T. Arima, and Y. Tokura, Magnetic control of ferroelectric polarization, Nature (London) **426**, 55 (2003).

[27] H. Katsura, N. Nagaosa, and A. V. Balatsky, Spin Current and Magnetoelectric Effect in Noncollinear Magnets, Phys. Rev. Lett. **95**, 057205 (2005).

[28] E. Sawaguchi and L. E. Cross, Spontaneous polarization of $Gd_2(MoO_4)_3$, J. Appl. Phys. **44**, 2541 (1973).

[29] P. E. Blöchl, Projector augmented-wave method, Phys. Rev. B **50**, 17953 (1994).

[30] G. Kresse and D. Joubert, From ultrasoft pseudopotentials to the projector augmented-wave method, Phys. Rev. B **59**, 1758 (1999); G. Kresse and J. Furthmüller, Efficient iterative schemes for *ab initio* total-energy calculations using a plane-wave basis set, Phys. Rev. B **54**, 11169 (1996).

[31] S. Nosé, A unified formulation of the constant temperature molecular dynamics methods, J. Chem. Phys. **81**, 511 (1984).

[32] D. M. Többens and W. Depmeier, Intermediate phases in the Ca-rich part of the system $(Ca_{1-x}Sr_x)_8[Al_{12}O_{24}](WO_4)_2$, Z. Kristallogr. **213**, 522 (1998).

[33] X. Hu, W. Depmeier, G. Wildermuth, and S. Doyle, New phase transitions in the solid solution system $(Ca_{1-x}Sr_x)_8[Al_{12}O_{24}](WO_4)_2$, Z. Kristallogr. **211**, 679 (1996).

[34] R. B. Olsen and D. Evans, Pyroelectric energy conversion: hysteresis loss and temperature sensitivity of a ferroelectric material, J. Appl. Phys. **54**, 5941 (1983).

[35] R. B. Olsen, D. A. Bruno, and J. M. Briscoe, Pyroelectric conversion cycles, J. Appl. Phys. **58**, 4790 (1985).

[36] E. Fatuzzo, H. Kiess, and R. Nitsche, Theoretical efficiency of pyroelectric power converters, J. Appl. Phys. **37**, 510 (1966).

[37] G. Sebald, E. Lefeuvre, and D. Guyomar, Pyroelectric energy conversion: Optimization principles, IEEE Trans. Ultrason. Ferroelectr. Freq. Control **55**, 538 (2008), and references therein.

[38] A. S. Mischenko, Q. Zhang, J. F. Scott, R. W. Whatmore, and N. D. Mathur, Giant electrocaloric effect in thin-film $PbZr_{0.95}Ti_{0.05}O_3$, Science **311**, 1270 (2006).

[39] A. S. Mischenko, Q. Zhang, R. W. Whatmore, J. F. Scott, and N. D. Mathur, Giant electrocaloric effect in the thin film relaxor ferroelectric $0.9PbMg_{1/3}Nb_{2/3}O_3$-$0.1PbTiO_3$ near room temperature, Appl. Phys. Lett. **89**, 242912 (2006).

[40] A. N. Morozovska, E. A. Eliseev, G. S. Svechnikov, and S. V. Kalinin, Pyroelectric response of ferroelectric nanowires: Size effect and electric energy harvesting, J. Appl. Phys. **108**, 042009 (2010).

[41] E. Cross, Materials science: Lead-free at last, Nature (London) **432**, 24 (2004).

[42] Y. Saito, H. Takao, T. Tani, T. Nonoyama, K. Takatori, T. Homma, T. Nagaya, and M. Nakamura, Lead-free piezoceramics, Nature (London) **432**, 84 (2004).